

Three-dimensional ionospheric conductivity associated with pulsating auroral patches: Reconstruction from ground-based optical observations

Mizuki Fukizawa¹, Yoshimasa Tanaka^{1, 2, 3}, Yasunobu Ogawa^{1, 2, 3}, Keisuke Hosokawa⁴, Tero Raita⁵,
5 Kirsti Kauristie⁶

¹National Institute of Polar Research, Tachikawa, 190-8518, Japan

²Polar Environment Data Science Center, Joint Support-Center for Data Science Research, Research Organization of Information and Systems, Tachikawa, 190-0014, Japan

³Department of Polar Science, The Graduate University for Advanced Studies (SOKENDAI), Tachikawa, 190-8518, Japan

10 ⁴Graduate School of Informatics and Engineering, University of Electro-Communications, Chofu, 182-8585, Japan

⁵Sodankylä Geophysical Observatory, University of Oulu, Oulu, FI-90014, Finland

⁶Finnish Meteorological Institute, Helsinki, FI-00101, Finland

Correspondence to: Mizuki Fukizawa (fukizawa.mizuki@nipr.ac.jp)

Abstract. Pulsating auroras (PsAs) appear over a wide area within the aurora oval in the midnight–morning–noon sector. In
15 previous studies, observations by magnetometers onboard satellites have reported the presence of field-aligned currents
(FACs) near the edges and interiors of pulsating aurora patches. PsAs are thus a key research target for understanding the
magnetosphere–ionosphere coupling process. However, the three-dimensional (3-D) structure of the electric currents has yet
to be clarified, since each satellite observation is limited to the single dimension along its orbit. This study’s aim was a
reconstruction of the 3-D structure of ionospheric conductivity, which is necessary to elucidate the 3-D ionospheric current.
20 Tomographic analysis was used to estimate the 3-D ionospheric conductivity for rapidly changing auroral phenomena such
as PsAs. The reconstructed Hall conductivity reached its maximum value of $1.4 \times 10^{-3} \text{ S m}^{-1}$ at 94 km altitude, while the
Pedersen conductivity reached its maximum value of $2.6 \times 10^{-4} \text{ S m}^{-1}$ at 116 km altitude. A secondary peak in the Pedersen
conductivity, due to electron-motion, at $9.9 \times 10^{-5} \text{ S m}^{-1}$ appears at 86 km altitude. The electron Pedersen conductivity
maximum value in the *D* region was approximately 38% of the ion Pedersen conductivity maximum value in the *E* region.
25 The FAC, derived under the assumption of a uniform ionospheric electric field, was approximately $70 \mu\text{A m}^{-2}$ near the edge
of the PsA patch. This FAC value was approximately 10 times that observed by satellites in previous studies. If the
conductivity around the patch is underestimated or the assumption of a uniform field distribution is incorrect, the FAC could
be overestimated. On the contrary, due to sharper boundary structures, the FAC could actually have had such a large FAC.

1 Introduction

30 Pulsating auroras (PsAs) are a kind of diffuse aurora with quasi-periodic luminosity modulation of $\sim 2\text{--}20$ s (Yamamoto,
1988). Although PsAs are dimmer in brightness than typical discrete auroras (some hundreds of Rayleigh (R) to tens of kR at

OI 557.7 nm; a few hundred R to ~ 10 kR at N_2^+ first negative band 427.8 nm) (McEwen et al., 1981; Royrvik and Davis, 1977), they are a general auroral phenomenon because of their wide range of appearance from the midnight to noon sectors depending on geomagnetic activities (Oguti et al., 1981; Royrvik and Davis, 1977). Typically, PsAs are typically grouped into three classes: auroral arcs, arc segments, and patches. This study focuses on patch-type PsAs.

Previous observations by satellite-borne magnetometers have indicated the occurrence of field-aligned currents (FACs) associated with PsA patches (Fujii et al., 1985; Gillies et al., 2015). Pairs of FACs flowing into and out of PsA patch edges are thought to be closed via the Pedersen current flowing within the PsA patch in the direction perpendicular to the geomagnetic field (Fujii et al., 1985; Oguti et al., 1984). PsAs are caused by precipitating electrons from a few keV to tens of keV scattered into the loss cone by whistler-mode chorus waves excited near the magnetic equator (Kasahara et al., 2018; Nishimura et al., 2010, 2011). Chorus waves, which propagate to the off-equator, scatter high-energy electrons from tens of keV to a few MeV and enhance the electron density in the ionospheric *D* region (Kawamura et al., 2021; Miyoshi et al., 2010, 2015, 2020, 2021; Shumko et al., 2021). Hosokawa and Ogawa (2010) investigated the altitude profile of the electron density obtained with the European Incoherent Scatter (EISCAT) radar, reporting that the Pedersen current carried by electrons was seen in the *D* region (at approximately 80–95 km altitudes) associated with PsAs in addition to the commonly seen ion Pedersen current in the *E* region (at an altitude of 120 km). They suggested that the electron Pedersen current in the *D* region contributed to FAC closure in the ionosphere because the PsA emission altitude was closer to the peak altitude of the electron Pedersen current layer than the ion Pedersen layer, even though the Pedersen conductivity in the *D* region was only $\approx 8 \times 10^{-5} \text{ S m}^{-1}$, a mere 13% that in the *E* region ($6 \times 10^{-4} \text{ S m}^{-1}$).

As mentioned above, the electric current structure associated with PsAs has been extensively studied by satellite and EISCAT radar observations. However, such observations are limited to the one dimension along the satellite's orbit or radar's beam direction. This is why the three-dimensional (3-D) structure of the current system has not yet been clarified. To elucidate the 3-D ionospheric currents, it is necessary to know the 3-D ionospheric conductivity and electric field. In the future the 3-D distribution of the ionospheric electric field will be obtained from the 3-D ion velocity vectors observed by the EISCAT_3D radar (<https://eiscat.se/>) (Stamm et al., 2023), which will begin observations in late 2023. On the contrary, it is difficult to obtain 3-D ionospheric conductivity measurement with high temporal and spatial resolutions for auroral phenomena given their high spatiotemporal variability, as seen in PsAs in particular.

This study aims to reconstruct the 3-D structure of the ionospheric conductivity associated with PsAs using computed tomographic analysis, a useful analysis method for measuring 3-D ionospheric physical quantities (Fukizawa et al., 2022). Generalized-Aurora Computed Tomography (G-ACT) is a method of reconstructing the two-dimensional electron flux and 3-D volume emission rate from monochromatic auroral images obtained with all-sky cameras (ASCs) at multiple locations (Aso et al., 2008; Tanaka et al., 2011). Fukizawa et al. (2022) demonstrated that the electron density altitude profile observed by the EISCAT radar could be reconstructed correctly using G-ACT. In this study, the 3-D Pedersen and Hall conductivities are reconstructed by combining a neutral atmosphere model and the 3-D electron density reconstructed by G-ACT.

65 2 Methods and Observations

2.1 Derivation of the three-dimensional ionospheric conductivity

The Pedersen conductivity σ_P and Hall conductivity σ_H can be written respectively as (Jones, 1974)

$$\sigma_P = \frac{en_e}{B} \left(\frac{\Omega_e v_{en}}{\Omega_e^2 + v_{en}^2} + \frac{\Omega_i v_{in}}{\Omega_i^2 + v_{in}^2} \right), \quad (1)$$

$$\sigma_H = \frac{en_e}{B} \left(\frac{\Omega_e^2}{\Omega_e^2 + v_{en}^2} - \frac{\Omega_i^2}{\Omega_i^2 + v_{in}^2} \right), \quad (2)$$

70 where e [C] is the elementary charge, n_e [m^{-3}] is the electron density, Ω_i and Ω_e [rad s^{-1}] are the ion and electron gyrofrequencies, respectively, and v_{in} and v_{en} [s^{-1}] are the ion-neutral and electron-neutral collision frequencies, respectively. v_{in} and v_{en} were estimated using the following equations (Brekke, 2013):

$$v_{in} = 4.34 \times 10^{-16} n(\text{N}_2) + 4.28 \times 10^{-16} n(\text{O}_2) + 2.44 \times 10^{-16} n(\text{O}), \quad (3)$$

$$v_{en} = 5.4 \times 10^{-16} [n(\text{N}_2) + n(\text{O}_2) + n(\text{O})] \cdot \sqrt{T_e}. \quad (4)$$

75 Here, $n(\text{N}_2)$, $n(\text{O}_2)$, and $n(\text{O})$ [cm^{-3}] are the ionospheric densities of nitrogen molecules, oxygen molecules, and oxygen atoms, respectively, and T_e [K] is the electron temperature. We assumed that the electron temperature could be approximated by the neutral temperature in the altitude range considered in this study when the electric field was not very high ($<30 \text{ mV m}^{-1}$) (Hosokawa and Ogawa, 2010). The neutral densities and temperature were taken from the Mass-Spectrometer-Incoherent-Scatter (MSIS)-E00 model (Picone et al., 2002).

80 2.2 Derivation of the three-dimensional electron density distribution

The origin of the simulation region was 69.4°N and 19.2°E . The z -axis was antiparallel to the geomagnetic field, the x -axis was antiparallel to the horizontal component of the geomagnetic field, and the y -axis was parallel eastward (see Fig. 2 in Tanaka et al. (2011)). The simulation region ranged from -75 to 75 km, from -100 to 100 km, and from 80 to 180 km for the x , y , and z axes, respectively. The spatial resolution was $2 \times 2 \times 2$ km.

85 We reconstructed the 3-D distribution of n_e in Eqs. (1) and (2) from auroral images using G-ACT, which reconstructs the electron flux from observed auroral images by maximizing the following posterior probability based on Bayes' theorem (Tanaka et al., 2011):

$$P(\mathbf{f}|\tilde{\mathbf{g}}) \propto \exp \left[-\frac{1}{2} \left\{ (\tilde{\mathbf{g}} - \mathbf{g}(\mathbf{f}))^T \Sigma^{-1} (\tilde{\mathbf{g}} - \mathbf{g}(\mathbf{f})) + \frac{\|\nabla^2 \mathbf{f}\|^2}{\sigma^2} \right\} \right]. \quad (5)$$

90 where \mathbf{f} [$\text{m}^{-2} \text{s}^{-1} \text{eV}^{-1}$] is the electron flux; $\tilde{\mathbf{g}}$ [R] is the brightness of the observed auroral image; $\mathbf{g}(\mathbf{f})$ [R] is the image brightness of the modeled auroral image; Σ^{-1} is the inverse covariance matrix; $\nabla^2 \mathbf{f}$ is the second-order derivative of \mathbf{f} with

respect to x , y , and E ; and σ^2 is the variance of $\nabla^2 \mathbf{f}$. The weights for derivatives in space and energy were set to 1. Here, we assumed that the pixel values in auroral images are mutually independent. In this case, the covariance matrix Σ is a diagonal matrix (i.e., the off-diagonal terms are zero) whose non-zero elements are the variance of each pixel value. The variance was determined from auroral images obtained with each ASC from 01:00 to 02:00 UT on February 18, 2018. The modeled
95 auroral image $\mathbf{g}(\mathbf{f})$ was obtained by integrating the 3-D volume emission rate along the line-of-sight direction from each pixel of each auroral image. The image brightness g_i at i -th pixel in the modeled auroral image was approximated as follows (e.g., Aso et al., 1990; Tanaka et al., 2011):

$$g_i = \frac{c_g(\theta, \phi)}{4\pi} \int L(r, \theta, \phi) dr, \quad (6)$$

where (r, θ, ϕ) are polar coordinates with origin at the center of the camera lens, and $c_g(\theta, \phi)$ is a sensitivity and vignetting
100 factor (Aso et al., 1990). The 427.8-nm and 557.7-nm volume emission rates were derived from the electron flux using the Global Airglow (GLOW) model (Solomon, 2017). The monoenergetic electron flux was specified in the GLOW model. We maximized $P(\mathbf{f}|\tilde{\mathbf{g}})$ in Eq. (5) by minimizing the following function:

$$\varphi(\mathbf{f}; \lambda, c_j) = \sum_j \left(c_j \tilde{\mathbf{g}}_j - \mathbf{g}_j(\mathbf{f}) \right)^T \Sigma_j^{-1} \left(c_j \tilde{\mathbf{g}}_j - \mathbf{g}_j(\mathbf{f}) \right) + \lambda^2 \|\nabla^2 \mathbf{f}\|^2 = \|\mathbf{r}(\mathbf{f}; \lambda, c_j)\|^2, \quad (7)$$

where

$$105 \quad \mathbf{r}(\mathbf{f}; \lambda, c_j) = \begin{pmatrix} \Sigma_j^{-\frac{1}{2}} \left(c_j \tilde{\mathbf{g}}_j - \mathbf{g}_j(\mathbf{f}) \right) \\ \lambda \nabla^2 \mathbf{f} \end{pmatrix}, \quad (8)$$

λ is the weighting factor for the spatial and energy derivative terms, and c_j is the correction factor for the relative sensitivity among ASCs. The subscript j is an index representing the various observation points. The method to determine these parameters is explained in Section 2.4.

We carried out the change of variables $\mathbf{f} = \exp(\mathbf{x})$ to take advantage of the non-negative constraint on the electron flux \mathbf{f}
110 (i.e., $\mathbf{f} \geq 0$). The initial value was obtained by minimizing the function $\varphi(\mathbf{x}; \lambda, c_j)$ by the Simultaneous Iterative Reconstruction Technique method (Gordon et al., 1970; Tanabe, 1971). We then minimized the function $\varphi(\mathbf{x}; \lambda, c_j)$ by implementing the Gauss–Newton (GN) method to reconstruct the electron flux and volume emission rate. In the GN method, the parameter \mathbf{x} was iterated according to $\mathbf{x}^{(k+1)} = \mathbf{x}^{(k)} + \Delta \mathbf{x}^{(k)}$. The step size at the k -th step was determined by solving the equation

$$115 \quad \left(\mathbf{J}^T(\mathbf{x}^{(k)}) \mathbf{J}(\mathbf{x}^{(k)}) \right) \Delta \mathbf{x}^{(k)} = -\mathbf{J}^T(\mathbf{x}^{(k)}) \mathbf{r}(\mathbf{x}^{(k)}), \quad (9)$$

where $\mathbf{J}(\mathbf{x})$ is the Jacobian matrix of $\mathbf{r}(\mathbf{x})$ with respect to \mathbf{x} . We solved Eq. (9) by the Conjugate Gradient (CG) method. The number of iterations of the CG method was set to 20. The criterion to stop the GN method was $\sqrt{\|\Delta\mathbf{x}^{(k)}/\mathbf{x}^{(k)}\|^2} < 10^{-2}$.

The reconstructed volume emission rate was converted to the electron density using the continuity equation of the electron density (Eq. (4) in Fukizawa et al. (2022)), i.e.,

$$120 \quad \frac{\partial n_e}{\partial t} = kL - \alpha_{\text{eff}}n_e^2, \quad (10)$$

where n_e [m^{-3}] is the electron density, L [$\text{m}^{-3} \text{s}^{-1}$] is the volume emission rate, k is a positive constant for converting the volume emission rate to the ionization rate (see Appendix B in Fukizawa et al. (2022)), and α_{eff} [$\text{m}^3 \text{s}^{-1}$] is the effective recombination rate. Eq. (10) was solved with the Runge–Kutta method. Using three effective recombination coefficients, Fukizawa et al. (2022) confirmed that the electron density observed by the European Incoherent Scatter (EISCAT) radar is

125 within the calculated electron densities.

2.3 Optical observations

We used monochromatic auroral images obtained with ASCs at 4 ground-based stations: Abisko (ABK: 68.36°N, 18.82°E), Kilpisjärvi (KIL: 69.05°N, 20.78°E), Skibotn (SKB: 69.35°N, 20.36°E), and Tromsø (TRO: 69.58°N, 19.22°E). ASCs to observe 427.8-nm auroral emission were installed at ABK, KIL, and SKB, while those for 557.7 nm were at KIL, SKB, and TRO. The field of view of each ASC at an altitude of 100 km is shown in Figure 1. ASCs for 427.8 nm at ABK and KIL

130 TRO. The field of view of each ASC at an altitude of 100 km is shown in Figure 1. ASCs for 427.8 nm at ABK and KIL were from the aurora observation network called Magnetometers Ionospheric Radars All-sky Cameras Large Experiment

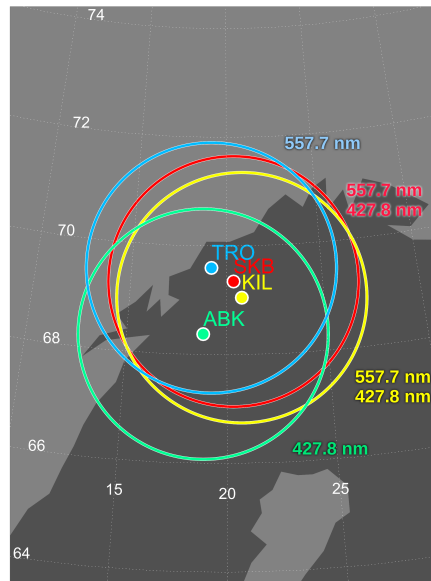


Figure 1. The field of views of all-sky cameras in Abisko (ABK), Kilpisjärvi (KIL), Skibotn (SKB), and Tromsø (TRO) at an altitude of 100 km. The map is over Northern Fennoscandia.

(MIRACLE) (Sangalli et al., 2011). The filter wavelength attached to the MIRACLE ASCs is 427.8 ± 2 nm. The other ASCs were Watec Monochromatic Imagers (WMIs) (Ogawa et al., 2020a). The filter wavelengths of WMIs were 430 ± 5 and 560 ± 5 nm. The pixel numbers were 512×512 pixels for MIRACLE ASCs and 640×480 pixels for WMIs. The exposure time was 1 s to observe 557.7-nm emission, but 2 s for dimmer 427.8-nm emission. The 557.7 nm auroral images were integrated every 2 s to match the time resolution of the 427.8-nm auroral images. To improve the signal-to-noise ratio, we composited 427.8-nm auroral images obtained from four same-type WMIs at SKB. In addition, the median filter of 3×3 pixels was applied to all auroral images. When the same median filter was applied to dark images subtracted from the auroral images, unexpected small structures appeared in the subtracted auroral images. To avoid this over-subtraction, we applied a 7×7 pixel median filter for the dark images. After the subtraction of the dark images, we conducted the flat field correction, Gamma correction, and conversion from count to Rayleighs. The relationship between count and Rayleighs can be written as the following equations.

$$[\text{Count}'] = 255 \times ([\text{Count}]/255)^{(1/\gamma)} \quad (11)$$

$$[\text{Rayleighs}] = a \times [\text{Count}'] + b \quad (12)$$

Here, Count is raw count, Count' is the Gamma-corrected count, γ is the Gamma value, and a and b are constants. The constants a and b were determined by the National Institute of Standards and Technology (NIST) traceable 1.9-m integration sphere (Labsphere LMS-760) at NIPR (Ogawa et al., 2020b). The parameters are summarized in Table 1.

Table 1. Filter wavelength and constants in Eqs. (11), (12), and (13) for each camera. c and d values are only for the 00:53:36 UT timepoint shown in Figure 4.

| Camera | Station | Filter wavelength (nm) | γ | a | b | c | d |
|---------|---------|------------------------|----------|-------|--------|-----|-------|
| MIRACLE | ABK | 427.8 ± 2 | 1.00 | 4.68 | 0.00 | 70 | 173 |
| MIRACLE | KIL | 427.8 ± 2 | 1.00 | 4.03 | 0.00 | 105 | 157 |
| WMI | SKB | 430 ± 5 | 0.45 | 20.95 | -17.65 | 80 | -386 |
| WMI | KIL | 560 ± 5 | 0.45 | 21.63 | 118.85 | 425 | -2516 |
| WMI | SKB | 560 ± 5 | 0.45 | 21.63 | 118.85 | 230 | -1204 |
| WMI | TRO | 560 ± 5 | 0.45 | 21.63 | 118.85 | 200 | -974 |

150 Figures 2a–f show, at each station and each wavelength, the keogram, which is the time series of the auroral image sliced along the magnetic longitude to pass through the pixel containing the EISCAT radar observation point from 00:45 to 01:20 UT on February 18, 2018. After an auroral breakup at 00:10 UT, diffuse auroras, PsAs, and auroral streamers were observed

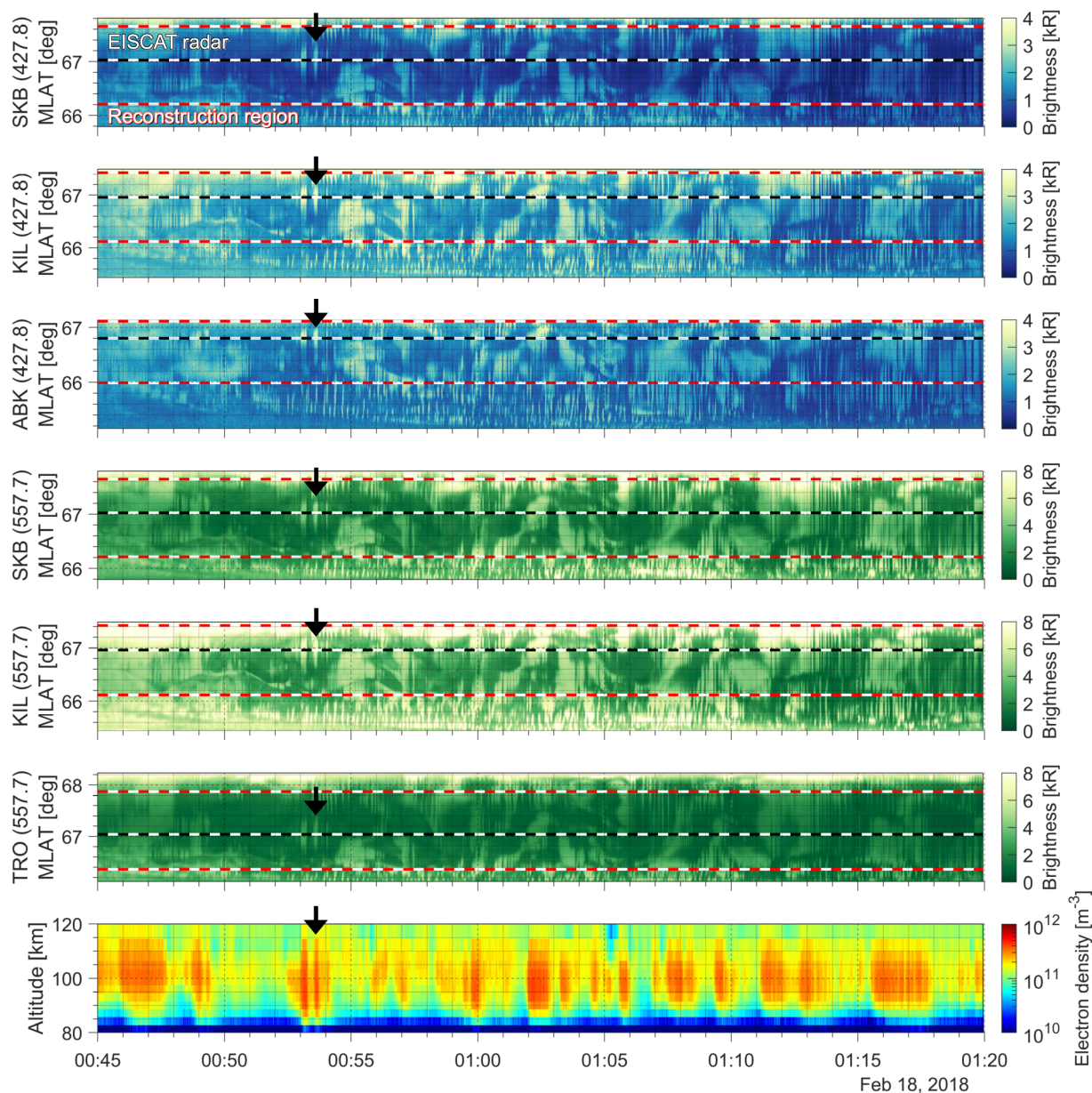


Figure 2. Keogram (time series of auroral image sliced along the magnetic longitude or north-south aligned direction to pass through the pixel containing the EISCAT radar observation point at 100 km altitude) at each station and each wavelength, from 00:45 to 01:20 UT on February 18, 2018. The vertical axis is the magnetic latitude (MLAT). Black and red dashed lines show the EISCAT radar observation point and reconstruction region, respectively. The bottom panel shows electron density observed by the EISCAT radar in Tromsø. Black arrows indicate the pulsating auroral patch analyzed in this study.

by ASCs at stations except for KIL (Video A1). It was cloudy at KIL until 00:47 UT. A PsA patch was detected at the EISCAT radar observation pixel at 00:53:30–00:53:42 UT, as shown by black arrows in Figure 2. The electron density increased in association with the PsA patch even below 85 km altitude (Figure 2). As shown in Figure 3, this PsA patch was classified as an expanding PsA, which expands from a core and then recedes back.

155 The PsA emissions in the auroral images were embedded in emissions such as diffuse aurora, sunlight, moonlight, and city light (Figures 4a–b). These background emissions, which have no specific structure, should be subtracted before conducting G-ACT because they cause ambiguity in the reconstruction results. The background emission image \mathbf{g}_{bk} was defined as

$$\mathbf{g}_{\text{bk}} = c\mathbf{g}_0 + d, \quad (13)$$

where \mathbf{g}_0 [R] is a modeled image derived by assuming all voxels had the same volume emission rate of $1 \text{ cm}^{-3} \text{ s}^{-1}$, $d =$
 160 $\min(\tilde{\mathbf{g}}) - \min(c\mathbf{g}_0)$, and c is a constant whose value is chosen to minimize $|\tilde{\mathbf{g}} - \mathbf{g}_{\text{bk}}|^2$. We did not use pixel values with zenith angle larger than 80° . The determined background emission profiles are shown with orange lines in Figure 4b. The values of c and d in Eq. (13) differ because the zenith angle of the sun or moon and the brightness of city light depend on the position of the observation point (Table 1). These values also varied with time due to temporal variation in diffuse auroral emission intensity. Figure 4c shows auroral images with background emission subtracted. The background removal could
 165 cause the underestimation of reconstructed volume emission rates if the background emission is dominated by diffuse auroral emission in the E region. This possibility is discussed in Section 4. Pixel values below 0 were set to 1 before tomographic analysis was performed.

Although the absolute value of the auroral image from each ASC has been corrected by calibration experiments in a
 170 laboratory, the images from different ASCs had different absolute values during actual observations due to differences in the sensitivity degradation and transmission of acrylic domes at each station. These differences were corrected by the parameter c_j in Eq. (7). The method to determine this parameter is explained in the next section.

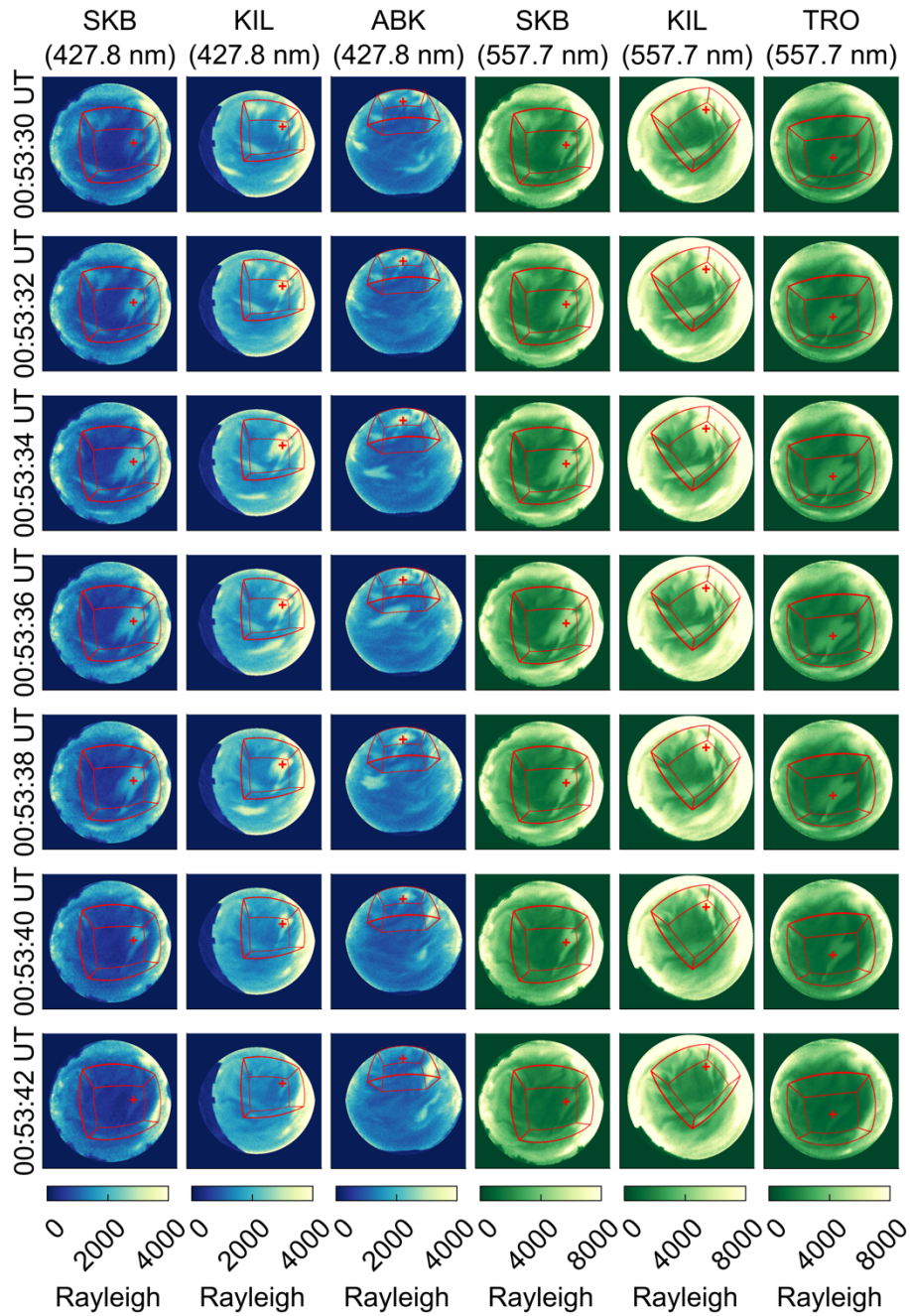


Figure 3. 427.8-nm and 557.7-nm auroral images obtained from all-sky cameras in Abisko (ABK), Kilpisjärvi (KIL), Skibotn (SKB), and Tromsø (TRO) from 00:53:30 to 00:53:42 UT on February 18, 2018. The red plus and lines represent the EISCAT radar observation pixel and reconstruction region boundaries, respectively.

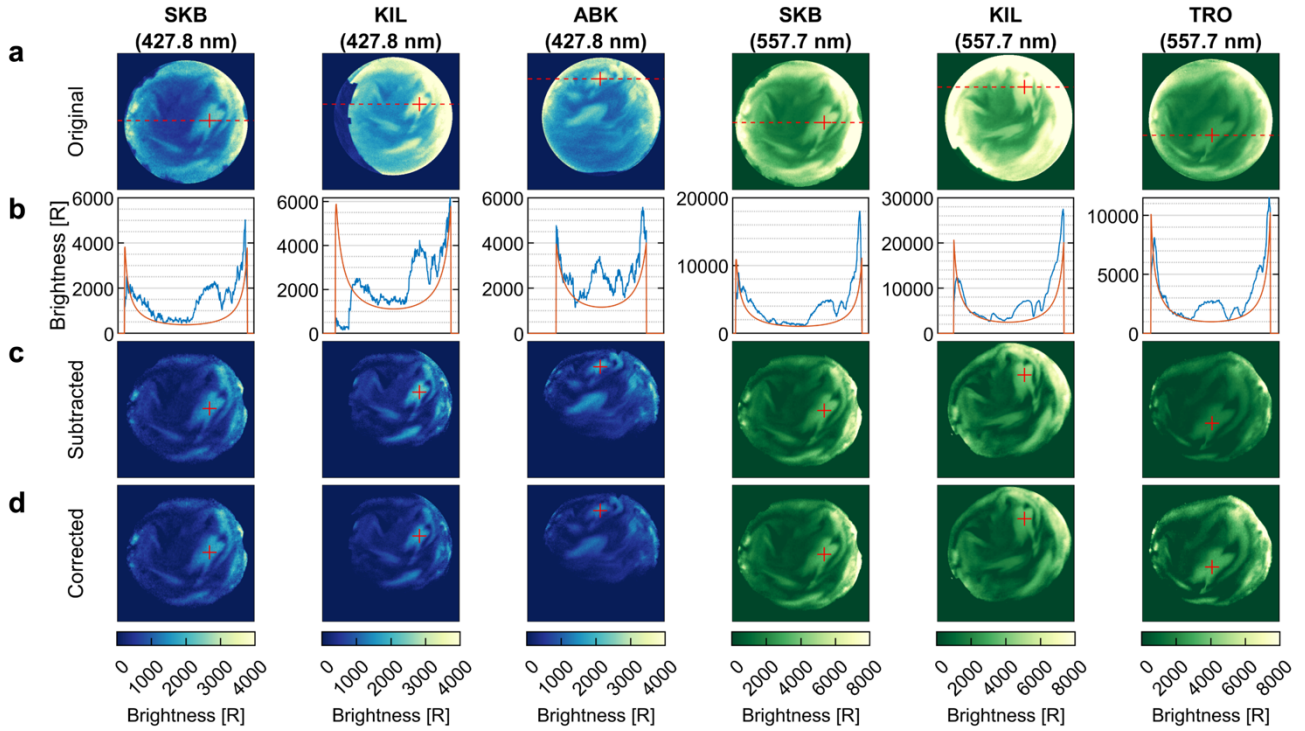


Figure 4. (a) Observed auroral images at 00:53:36 UT on February 18, 2018. Red pluses represent EISCAT radar observation pixels. (b) Brightness of observed auroral images (blue lines) and estimated background emission (orange lines) along red dashed lines in Figure 4a. (c, d) Auroral images with (c) background emission subtracted and (d) relative sensitivity corrected.

175 2.4 Determination of hyperparameters

Before conducting G-ACT, the hyperparameters λ and c_j in Eq. (7) must be determined. First, we determined c_j ($j = 1, 2, \dots, 6$) with λ fixed at 10^{-5} using fivefold cross-validation (Stone, 1974). Elements of the observed auroral image vector $\tilde{\mathbf{g}}$ were divided into five subsets. Then, one subset was selected as the test set ($\tilde{\mathbf{g}}_j^{\text{tes}}$) and the others as the training set ($\tilde{\mathbf{g}}_j^{\text{tra}}$). We found the solution $\hat{\mathbf{x}}$ to minimize $\varphi(\mathbf{x}; \lambda, c_j)$ using only the training set $\tilde{\mathbf{g}}_j^{\text{tra}}$ and then predicted the test set $\mathbf{g}_j^{\text{tes}}(\hat{\mathbf{x}})$. We then

180 calculated the residual sum of squares between the actual and predicted values for the test data:

$$\delta(c_j) = \sum_j \|c_j \tilde{\mathbf{g}}_j^{\text{tes}} - \mathbf{g}_j^{\text{tes}}(\hat{\mathbf{x}})\|^2. \quad (14)$$

The cross-validation score $\bar{\delta}(c_j)$ was calculated by averaging over five values of $\delta(c_j)$, which were obtained by using a different set as the training set each time. To save computational cost, cross-validation was performed separately for each wavelength. The relative sensitivities of SKB were fixed to be 1 for each wavelength, while the other relative sensitivities

185 were determined using the grid search method. The determined values were 0.78 for ABK (427.8 nm), 0.73 for KIL (427.8

nm), 0.61 for KIL (557.7 nm), and 1.92 for TRO (557.7 nm). Auroral images with relative sensitivity corrected are shown in Figure 4d.

The value of the parameter λ was selected so as to minimize the difference between the electron densities observed by the EISCAT radar and those reconstructed by G-ACT. We conducted G-ACT for $\lambda = 10^{-5}, 10^{-4}, 10^{-3}, 10^{-2}, 10^{-1}$, and 10^0 and found that the difference reached a minimum at $\lambda = 10^{-1}$.

2.5 Validation of reconstruction accuracy using model aurora

In Fukizawa et al. (2022), PsA patches were reconstructed using only 427.8-nm auroral images at three stations (ABK, KIL, and TRO). By contrast, we improved the G-ACT method by adding auroral images at another wavelength (557.7 nm) at three stations (KIL, SKB, and TRO). The total number of stations was increased from three to four due to the addition of TRO. We performed G-ACT for a model aurora to determine the extent of reconstruction accuracy improvement associated with including the additional wavelength and observation point. First, horizontal distributions of total energy flux and average energy were prepared for three adjacent patches. The total energy flux was assumed to have a Gaussian distribution with a peak value of 1.6 mW m^{-2} (Figure 5a). A uniform distribution with a value of 30 keV was assumed for the average

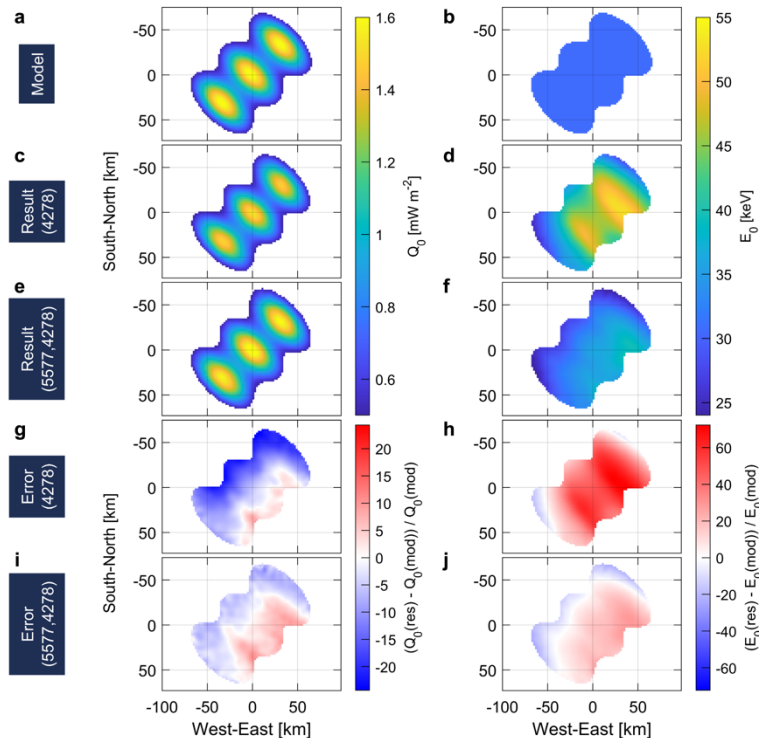


Figure 5. Models of (a) the total energy flux Q_0 and (b) average energy E_0 . (c–f) Reconstructed results of (c, e) the total energy flux and (d, f) average energy using (c, d) only 427.8-nm auroral images or (e, f) both 557.7-nm and 427.8-nm auroral images. (g–j) Relative reconstruction errors calculated as (Result – Model) / Model.

Table 2. Errors of the total energy flux (Q_0) and average energy (E_0) reconstructed using only 427.8-nm auroral images vs. using both 557.7-nm and 427.8-nm auroral images. Error ranges and average errors are listed. The errors were calculated as (Result – Model) / Model.

| | Error range | | Average error |
|--------------------------|-------------|-----|---------------|
| Q_0 (427.8 nm) | -24% | 10% | -8% |
| Q_0 (557.7 & 427.8 nm) | -11% | 11% | -0.6% |
| E_0 (427.8 nm) | -19% | 72% | 36% |
| E_0 (557.7 & 427.8 nm) | -25% | 29% | 7% |

energy (Figure 5b). Second, the 3-D distributions of the volume emission rate at wavelengths of 427.8 nm and 557.7 nm were derived using the GLOW model. Third, modeled auroral images were obtained by integrating the 3-D volume emission rates from the various observation points. Random noises from a normal distribution with a mean value of 0 and standard deviation determined from observed auroral images were added to the modeled images. Fourth, the total energy flux and average energy were reconstructed using only 427.8-nm images (Figures 5c–d) and using both 557.7 and 427.8 nm images (Figures 5e–f). Finally, relative errors between the reconstructed and modeled total energy flux and between the reconstructed and modeled average energy were calculated as Error = (Result – Model) / Model (Figures 5g–j). The total energy flux and average energy were underestimated in the northwest and overestimated in the southeast, but the use of auroral images at both 557.7 nm and 427.8 nm showed a decrease in error compared to the use of only the 427.8 nm images. Error ranges and average errors for the total energy flux and average energy are listed in Table 2.

3 Results

3.1 G-ACT reconstruction results

The precipitating electron fluxes and volume emission rates at wavelengths of 557.7 nm and 427.8 nm were reconstructed from auroral images using G-ACT. Figure 6 depicts the total energy flux and average energy of the reconstructed precipitating electron flux. The total energy flux reached its maximum value of $\sim 2.5 \text{ mW m}^{-2}$ near the center part of the PSA patch from 00:53:34 to 00:53:38 UT. The average energy reached its maximum value of $\sim 62 \text{ keV}$ at 00:53:38 UT.

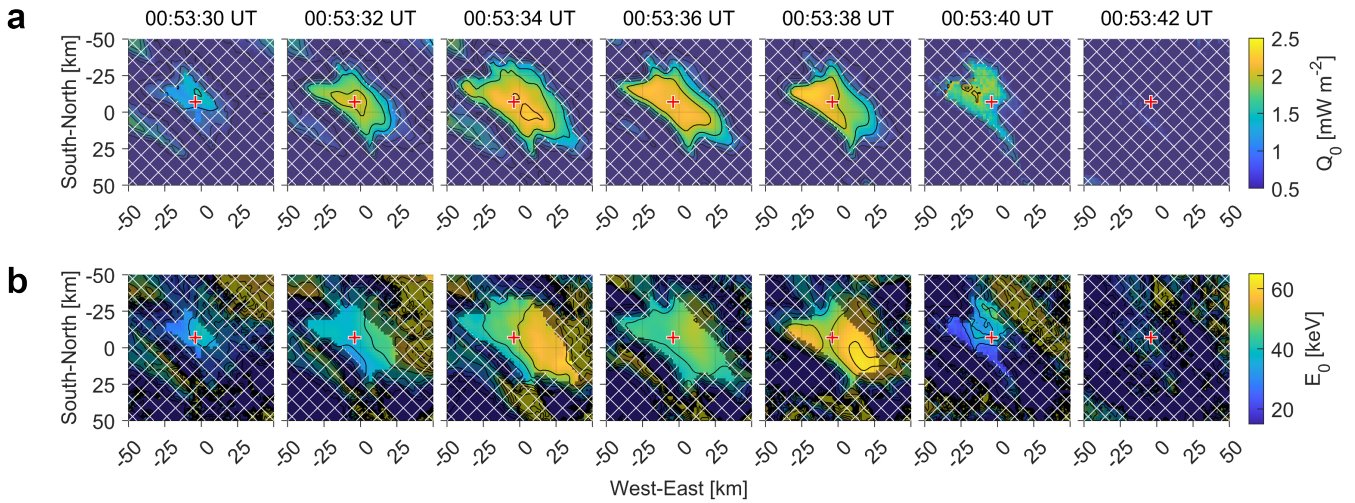


Figure 6. (a) The total energy flux Q_0 and (b) average energy E_0 of the reconstructed electron flux. The pixels where the total energy flux was less than 1.0 mW m^{-2} are hatched by white lines. Red pluses represent the EISCAT radar observation point.

215 Figures 7 and 8 illustrate the 3-D distribution of the reconstructed volume emission rate at wavelengths of 557.7 nm and
 427.8 nm, respectively. The peak altitudes of the volume emission rate along the EISCAT radar beam were approximately
 94 km for 557.7 nm and 86 km for 427.8 nm (Figures 7c, 7d, 8c, and 8d). To validate the G-ACT reconstruction results, the
 difference between the observed auroral image (Figure 9a) and the modeled auroral image (Figure 9b) obtained by
 220 integrating the reconstructed volume emission rates from the various stations was calculated and is shown in Figure 9c. The
 observed auroral images were almost perfectly reconstructed except for images at ABK, for which the reconstruction region
 lay near the edge of the ASC's field of view. One of the reasons for this error was that the ground stations were biased to the
 south of the analyzed PsA patch. Therefore, increasing the number of observation points from the north or targeting an
 auroral structure closer to the centroid of the observation points is expected to mitigate this error.

225

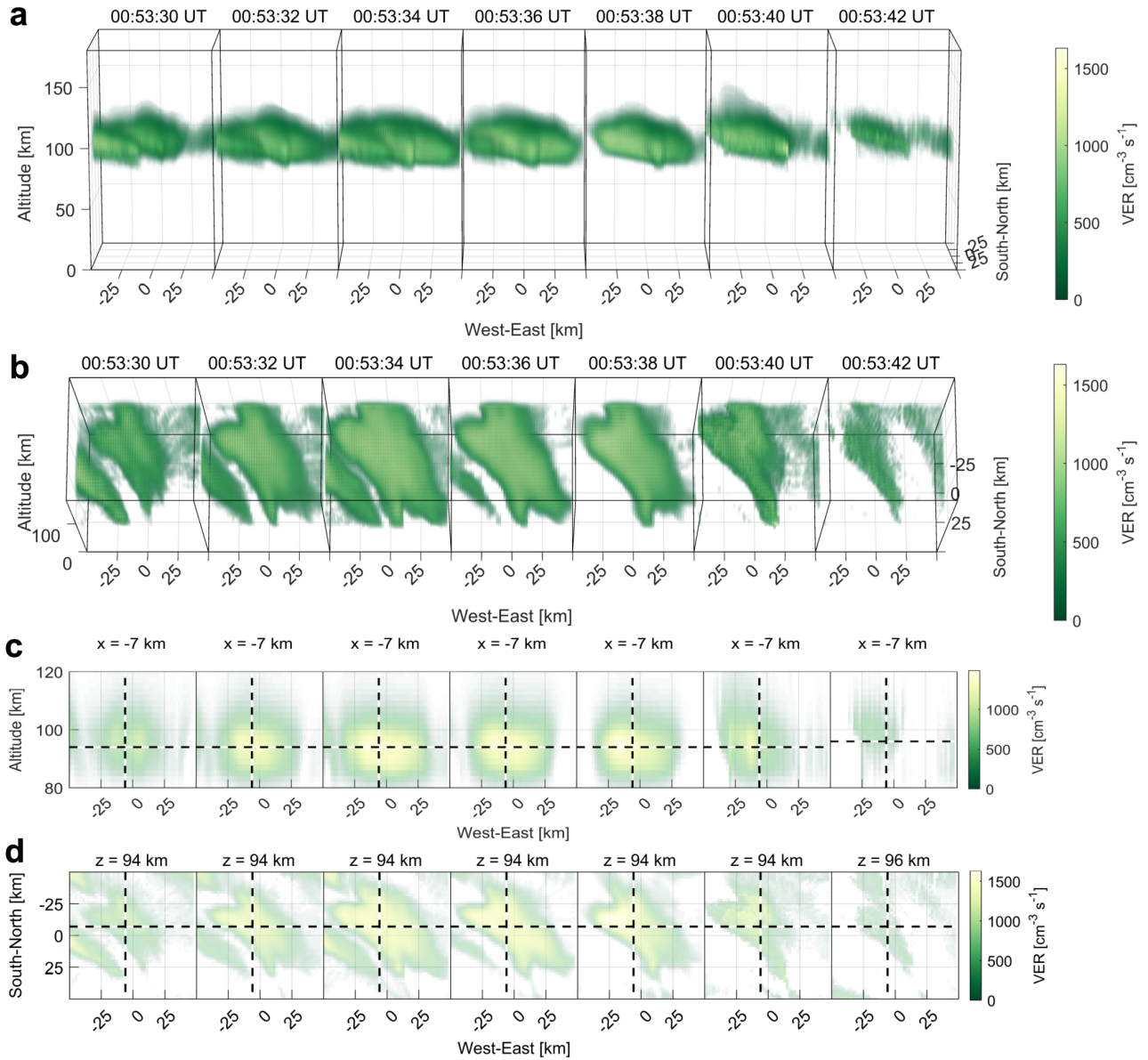


Figure 7. (a, b) The 3-D distribution of the reconstructed volume emission rate (VER) at a wavelength of 557.7 nm viewed from different elevation angles. (c) Cross-sections parallel to the magnetic field lines and (d) horizontal cross-sections containing peak values on the EISCAT radar beam. Vertical and horizontal dashed lines show the EISCAT radar beam and the altitude of peak volume emission rate, respectively. The transparency depends on the VER values. The minimum VER is invisible and the maximum VER is opaque.

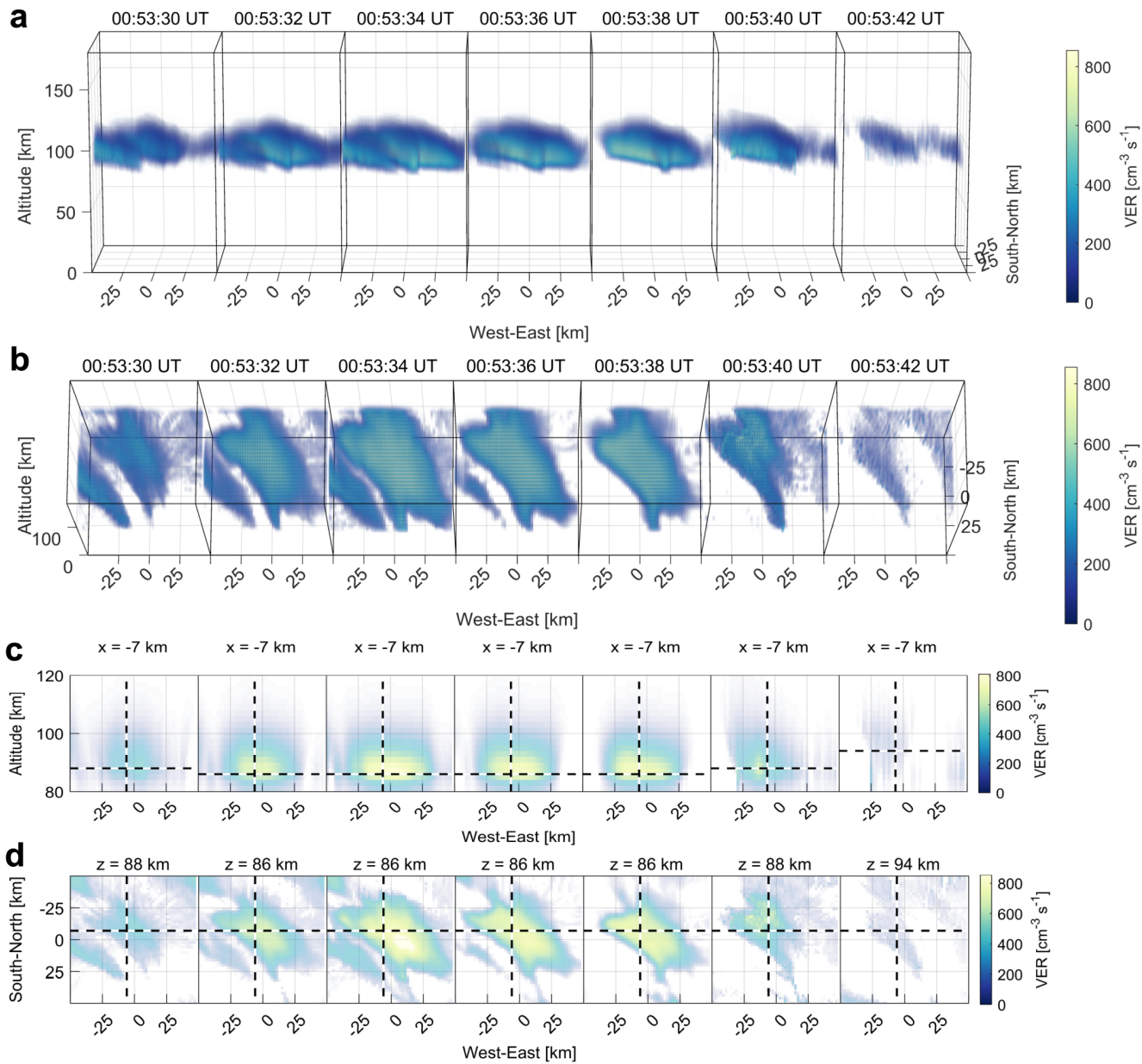


Figure 8. The reconstructed volume emission rate at a wavelength of 427.8 nm. Figure format is the same as that of Figure 7.

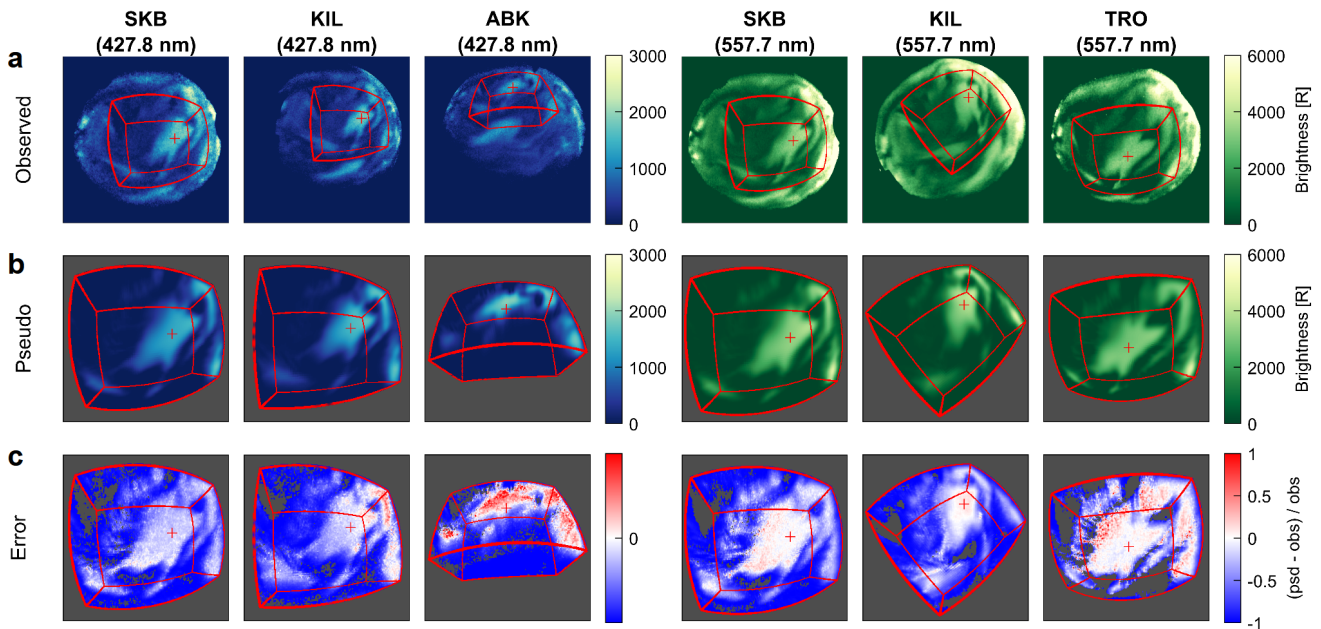


Figure 9. (a) Observed auroral images at 00:53:36 UT on February 18, 2018. Red pluses and lines represent the EISCAT radar observation pixel and the reconstruction region boundaries, respectively. (b) Modeled auroral images, calculated from the reconstructed volume emission rate. (c) Relative errors, calculated as $[(b) - (a)] / a$. Errors with observed auroral brightness was less than 100 are not shown.

230 3.2 Three-dimensional Pedersen and Hall conductivities

As explained in Section 2.2, the electron density was derived from the reconstructed volume emission rate at 427.8 nm (Figure 8) using the Runge–Kutta method to solve the continuity equation of the electron density (Eq. (10)). Figure 10 depicts the reconstructed 3-D electron density. The effective recombination coefficient used was (Gledhill, 1986)

$$\alpha_{\text{fit}} = 4.30 \times 10^{-12} \exp(-2.42 \times 10^{-2} z) + 8.16 \times 10^6 \exp(-0.524 z) \quad [\text{m}^3 \text{s}^{-1}], \quad (15)$$

235 where z [km] is the altitude. Gledhil (1986) derived Eq. (15) using the least-squares method for 122 data points of the effective recombination coefficient obtained from 18 previous studies (references in Gledhil, 1986). The peak electron density on the EISCAT radar beam occurred at an altitude of almost 94–96 km (Figs. 10c and 10d). The method of solving the continuity equation of the electron density accounted for time variation and thus was able to show that the electron density remained high even after the brightness of the aurora faded at 00:53:42 UT. To evaluate the reconstruction accuracy

240 of the electron density, the reconstructed altitudinal profile of electron density was compared with that observed by the EISCAT radar (Figure 11a). In addition to the effective recombination coefficient of Eq. (15), two coefficients were used as the upper and lower bounds on α_{eff} in Eq. (10) (Semeter and Kamalabadi, 2005), namely,

$$\alpha_{\text{NO}^+} = 4.2 \times 10^{-13} (300/T_n)^{0.85} \quad [\text{m}^3 \text{s}^{-1}], \quad (16)$$

$$\alpha_{O_2^+} = 1.95 \times 10^{-13} (300/T_n)^{0.7} \quad [\text{m}^3 \text{s}^{-1}], \quad (17)$$

245 where T_n [K] is the neutral temperature. The observed electron densities lay mostly within the electron density distribution obtained using the three effective recombination coefficients. Especially, below about 90 km altitude, the electron density calculated using Eq. (15) was the most consistent with the observed electron density. Therefore, we used Eq. (15) to

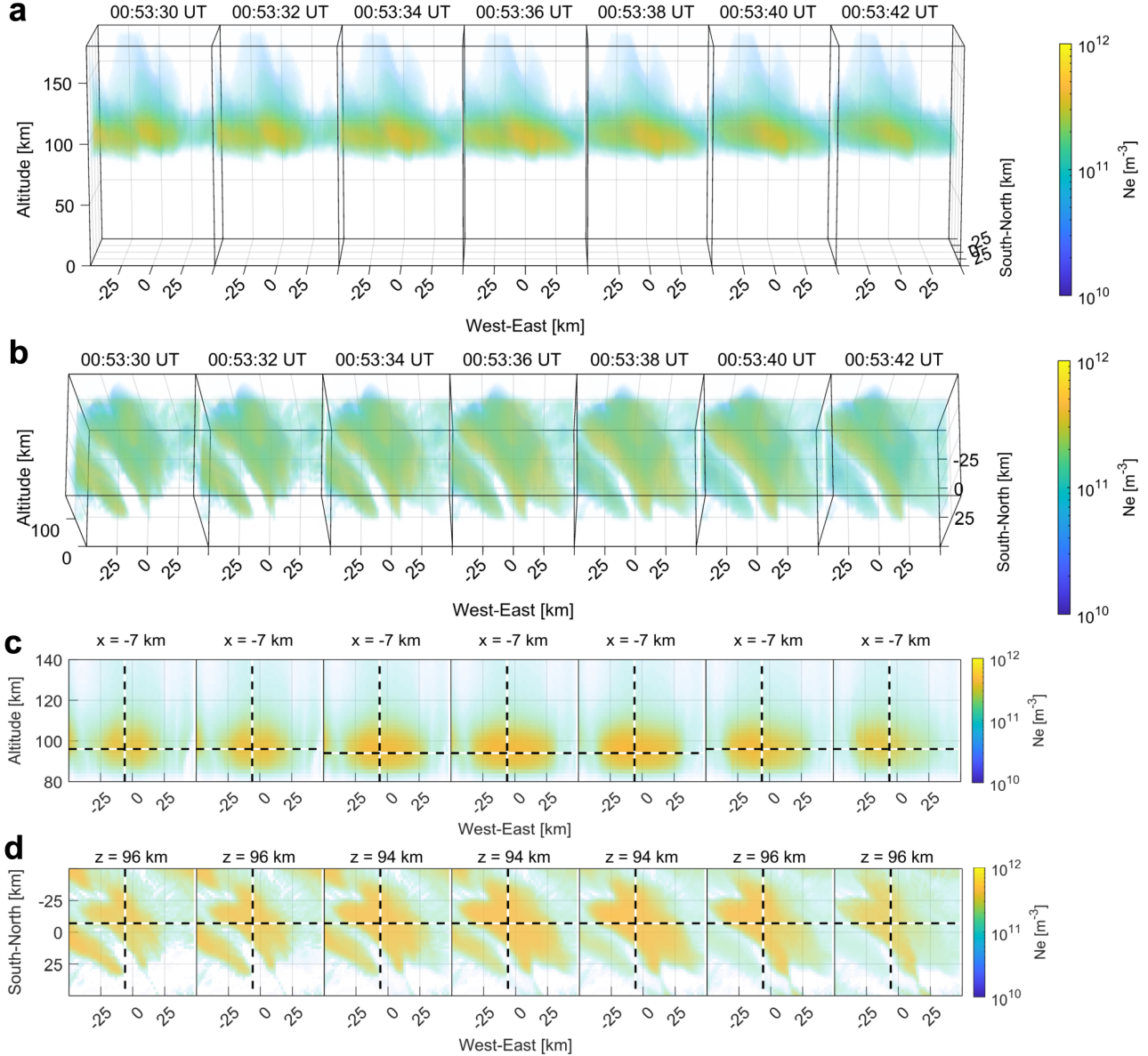


Figure 10. (a, b) Reconstructed 3-D electron density (N_e) viewed from different elevation angles. (c) Cross-sections parallel to the magnetic field lines and (d) horizontal cross-sections containing peak values on the EISCAT radar beam. Vertical and horizontal dashed lines represent the EISCAT radar beam and the altitude of peak electron density, respectively.

calculate the electron density in Fig. 10. The Pedersen and Hall conductivities were calculated by substituting the reconstructed electron density (Fig. 10) into Eqs. (1) and (2). Figures 12 and 13 illustrate the 3-D distribution of the reconstructed Hall and Pedersen conductivities. The Hall conductivity reached its maximum value of $1.4 \times 10^{-3} \text{ S m}^{-1}$ at 94 km altitude, while the Pedersen conductivity reached its maximum value of $2.6 \times 10^{-4} \text{ S m}^{-1}$ at 116 km altitude. The Pedersen conductivity showed a secondary peak of $9.9 \times 10^{-5} \text{ S m}^{-1}$ at 86 km altitude. The electron Pedersen conductivity maximum value in the *D* region was approximately 38% of the ion Pedersen conductivity maximum value in the *E* region, compared to a figure of 13% in Hosokawa and Ogawa (2010). The altitude profiles of the reconstructed Hall and Pedersen conductivities were compared with those calculated from the electron densities observed by the EISCAT radar (Figures 11b and 11c). Although the Pedersen conductivity values reconstructed by G-ACT were overestimated in the *D* region compared to those of the EISCAT radar by a factor of 1.2–1.5, the *D*-region Pedersen conductivity peak values derived from the EISCAT radar were also 25–44% of those in the *E* region, in keeping with the G-ACT results.

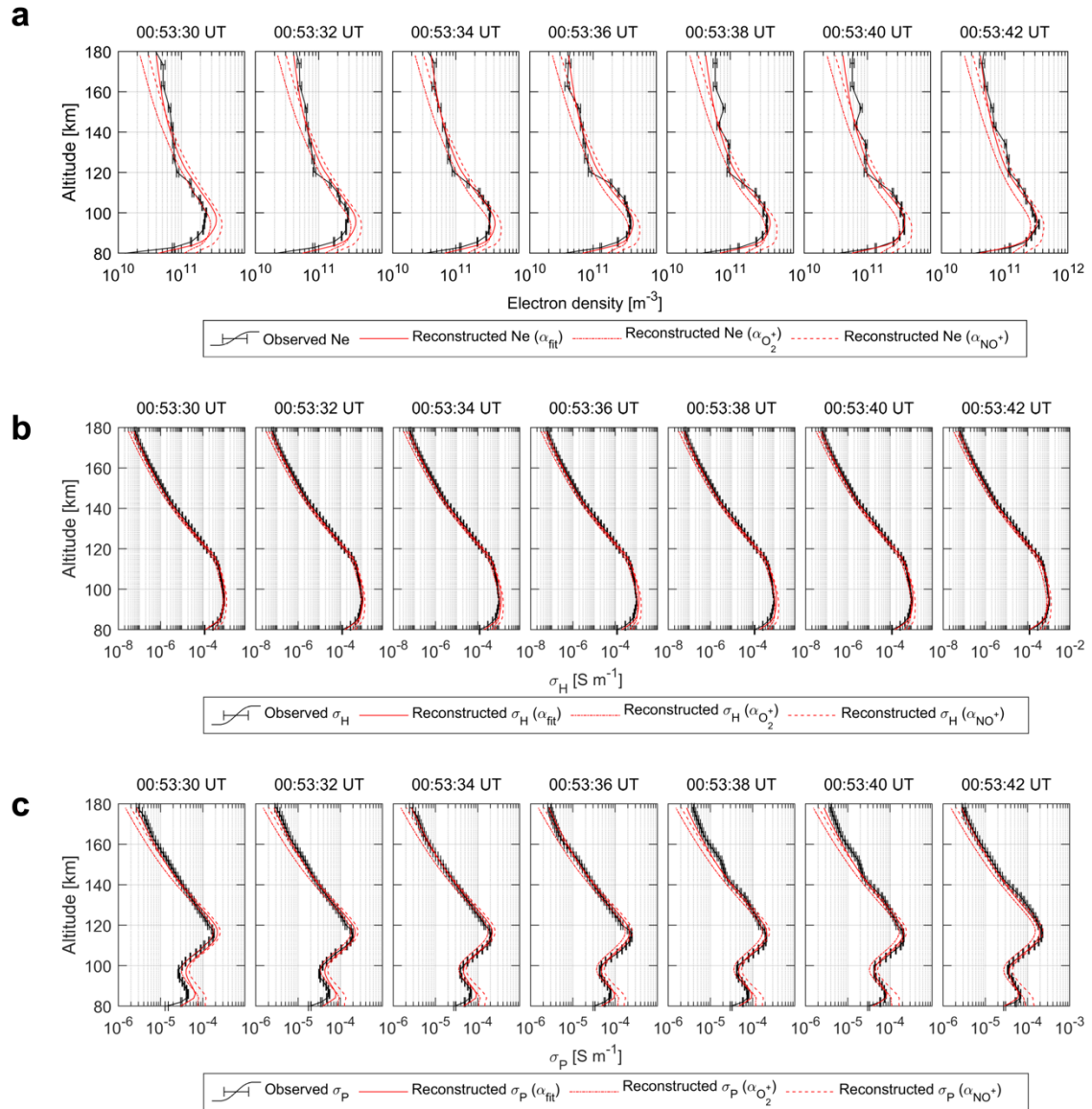


Figure 11. Altitude profiles of the reconstructed (red lines) and observed (black lines) (a) electron density, (b) Hall conductivity, and (c) Pedersen conductivity. Error bars represent measurement uncertainties.

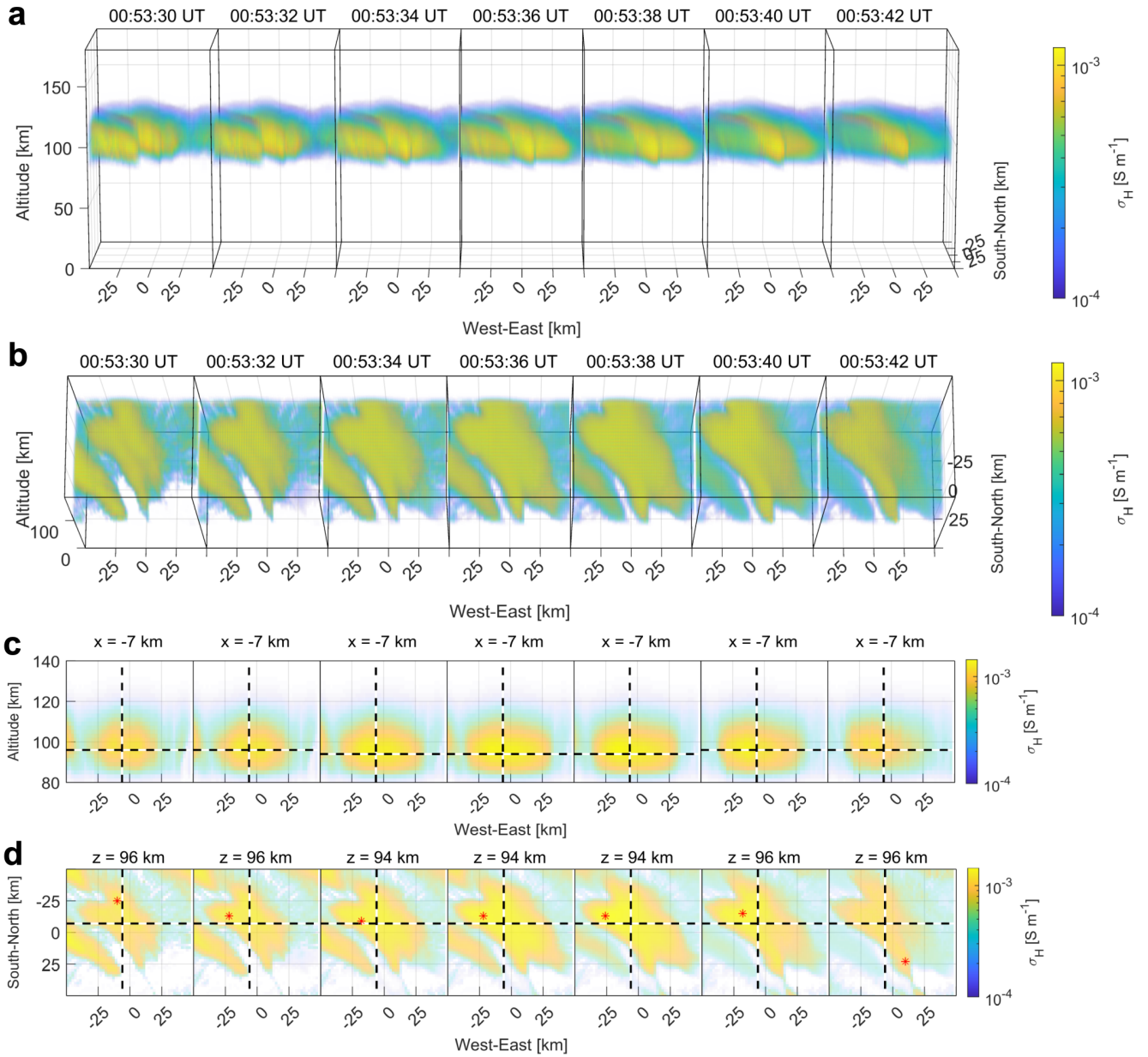


Figure 12. (a, b) The 3-D distribution of the reconstructed Hall conductivity. (c) Cross-sections parallel to the magnetic field lines and (d) horizontal cross-section containing peak values on the EISCAT radar beam. Vertical and horizontal dashed lines show the EISCAT radar beam and the altitude of peak Hall conductivity, respectively. Red asterisks represent peak value positions within the center of the PsA patch.

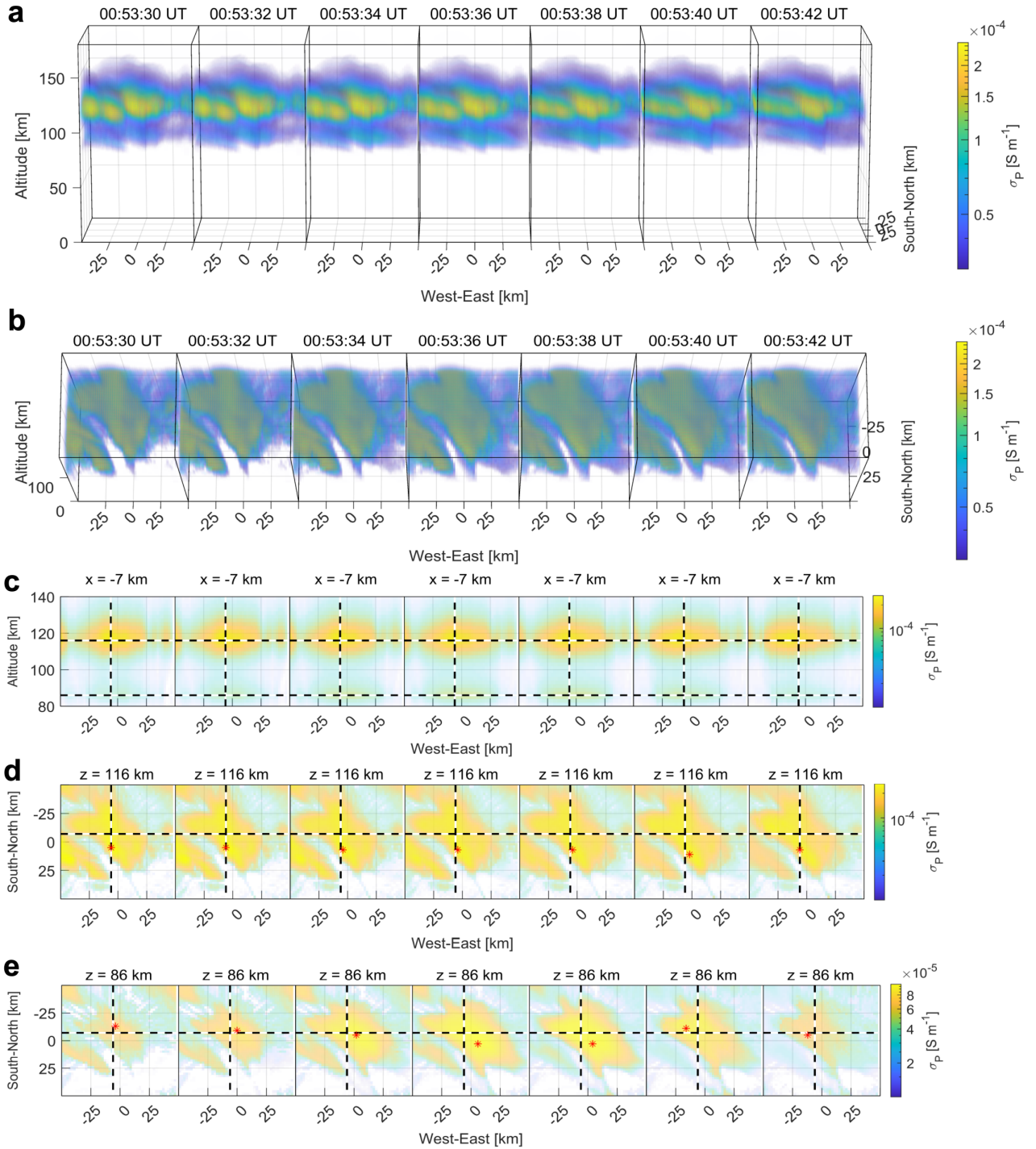


Figure 13. The 3-D distribution of the reconstructed Pedersen conductivity. The figure format is the same as that of Figure 12.

4 Discussion

265 The horizontal distribution of the Pedersen conductivity in the D region varied significantly in space and time compared to
 the E region (Figs. 13d and 13e). The peak location in horizontal planes differed between the electron and ion Pedersen
 layers. These altitudinal differences in the horizontal distribution of the Pedersen conductivity affect the closure of FACs
 associated with PsAs. It is expected that in the future, the ionospheric conductivity obtained using the method proposed in
 this study will be combined with EISCAT_3D data to elucidate how the FACs associated with PsAs are closed in the
 270 ionosphere.

3-D electric field data, which will be obtained in the future by EISCAT_3D radar observations, are not available at present.
 However, the electric field is often assumed to be uniform around PsAs, since PsA patches often drift uniformly with the
 $\mathbf{E} \times \mathbf{B}$ drift velocity (Hosokawa et al., 2010; Hosokawa and Ogawa, 2010; Oguti et al., 1984; Yang et al., 2015). Therefore,
 we evaluated the amount of FAC caused solely by the non-uniform distribution of ionospheric conductivity under the
 275 assumption of a uniform electric field. According to current continuity, the FAC, j_{\parallel} [A m^{-2}], is equal to the divergence of the
 height-integrated current perpendicular to the magnetic field lines, J_{\perp} [A m^{-1}]. Using the current continuity and ionospheric
 Ohm's law, the FAC can be written as

$$j_{\parallel} = \nabla_{\perp} \cdot J_{\perp} = (\nabla_{\perp} \Sigma_P) \cdot \mathbf{E}_{\perp} + \Sigma_P (\nabla_{\perp} \cdot \mathbf{E}_{\perp}) - (\nabla_{\perp} \Sigma_H) \cdot (\mathbf{E}_{\perp} \times \mathbf{b}) - \Sigma_H \mathbf{b} \cdot (\nabla_{\perp} \times \mathbf{E}_{\perp}), \quad (18)$$

where Σ_P and Σ_H [S] are the height-integrated Pedersen and Hall conductivities, respectively, \mathbf{E}_{\perp} [V m^{-1}] is the ionospheric
 280 electric field perpendicular to the magnetic field, and \mathbf{b} is the unit vector of the geomagnetic field. We assumed a uniform
 southward \mathbf{E}_{\perp} , allowing the second and fourth terms in Eq. (18) to be ignored. The \mathbf{E}_{\perp} amplitude was estimated to be 12.5
 mV m^{-1} from the ionospheric convection velocity obtained from Super Dual Auroral Radar Network (SuperDARN)
 (Greenwald et al., 1995) observations ($\sim 250 \text{ m s}^{-1}$) and assuming $B \approx 50000 \text{ nT}$. Consequently, the maximum downward
 and upward FACs were 69 and $68 \text{ } \mu\text{A m}^{-2}$ at the northeast and southwest edges of the PsA patch, respectively. These FACs
 285 are approximately ten times larger than those observed by magnetometers onboard satellites (Gillies et al., 2015). It is
 possible that the PsA patches analyzed in this study actually had such large FACs, given that their boundaries were sharper
 than those of Gillies et al. (2015). Gillies et al. (2015) may also have underestimated the FAC by $\sim 50 \text{ } \mu\text{A m}^{-2}$ around 67°
 magnetic latitude, where the PsA patch was detected in this study, according to Figure 4 in Ritter et al (2013). If our results
 are overestimated, mainly there are two main factors. One is that the uniform \mathbf{E}_{\perp} assumption may not be reasonable. Indeed,
 290 higher conductivities drive the polarization of the electric field inside PsA patches (Hosokawa et al., 2010; Takahashi et al.,
 2019). The 3-D distribution of the ionospheric electric field will be obtained with the EISCAT_3D radar in the near future,
 settling this question. The other factor is the background emission subtraction from the auroral images before conducting G-
 ACT. Background emission subtraction enabled accurate reconstruction within the PsA patch. However, the conductivity

outside the patch will be underestimated if the subtracted background emission contains mainly diffuse auroral emission. On
295 the contrary, if uniform diffuse auroral emission occurs around 150 km altitude, above PsAs, as reported by Brown et al.
(1976), then the subtraction is not a problem because the horizontal gradient of electrical conductivity near the PsA patch is
not affected by the subtraction. The peak altitude of auroral emissions or the characteristic energy of precipitating electrons
can be estimated from the emission intensity ratio of 557.7–427.8 nm (Rees and Luckey, 1974; Steele and McEwen, 1990).
The intensity ratio of the removed background emission at 557.7/427.8 was 2.8. This ratio indicates that the characteristic
300 energy of the precipitating electrons was 1.6–4.0 keV (Figure 4 in Rees and Luckey (1974)), ~1.5–5 keV (Figure 9 in Steele
and McEwen (1990)), or ~20 keV using the GLOW model. Thus, the characteristic energy derived from the 557.7/427.8 ratio
depends on the models. The background emission intensity subtracted in our analysis was about 30% of the observed
pulsating auroral emission. Therefore, the volume emission rate of the background emission was calculated using the GLOW
model and multiplied by a constant so that the ratio of the linearly integrated volume emission rate in the altitude direction is
305 30% of the volume emission rate of the reconstructed pulsating aurora. Then, the electron density was derived using the
electron continuity equation by adding the calculated background emission to the reconstructed volume emission rate. We
examined how much the electron density is underestimated at altitudes of 86, 96, and 116 km, where the Pedersen and Hall
conductivities show peak values. For a characteristic energy of 1 keV, the electron density was underestimated by ~30-40%
at an altitude of 116 km and remained the same at altitudes of 86 km and 96 km. When the characteristic energy was 20 keV,
310 the underestimation was ~10% at all three altitudes. The horizontal distribution of the ionospheric conductivity around PsA
patches will be investigated by the EISCAT_3D radar in the near future.

5 Conclusions

In this study, G-ACT was used to reconstruct the 3-D distributions of the Hall and Pedersen conductivities of PsAs in order
to elucidate the 3-D structures of ionospheric currents. The tomographic results show that the Hall conductivity peaked in the
315 *E* region (altitudes of 94–96 km) while the Pedersen conductivity peaked in the *E* region (at 116 km altitude) with a
secondary peak in the *D* region (at 86 km altitude). The electron Pedersen conductivity maximum value in the *D* region was
approximately 38% of the ion Pedersen conductivity maximum value in the *E* region; this ratio was nearly triple that
reported by Hosokawa and Ogawa (2010). This result suggests that the Pedersen current in the *D* region caused by high-
energy electron precipitation associated with PsAs has an outsized effect on FAC closure in the ionosphere.
320 Under the assumption of a uniformly distributed ionospheric electric field, derived FAC values near the edges of PsA
patches were approximately ten times higher than those reported by satellite observations. This overestimation means that
the ionospheric electric field is not uniform and that the electrical conductivities around PsA patches may be underestimated.
In the near future, the 3-D ionospheric conductivity reconstruction using G-ACT proposed in this study will be combined
with 3-D observations of ionospheric conductivity and electric field strength by EISCAT_3D radar to elucidate the 3-D
325 ionospheric current structures associated with PsAs.

Data availability

The MIRACLE EMCCD camera data from ABK and KIL are available at ***. The auroral images obtained by the four WMI CCD cameras can be obtained at ***. The EISCAT data can be accessed from <http://esr.nipr.ac.jp/www/eiscatdata/>.

330 The SuperDARN data can be found at ***. (The data used in this study will be prepared for open access when the manuscript is accepted.)

Video supplement

We will get a DOI for Video A1 when this manuscript is accepted. Currently, it is available from the following link: https://www.dropbox.com/s/tzy104lannpgewa/Video_A1.mp4?dl=0.

335 **Author contribution**

Yoshimasa Tanaka developed the G-ACT method and code. Yasunobu Ogawa conducted the EISCAT radar observation and prepared the ionospheric electron density data. Tero Raita maintained the MIRACLE camera network and prepared the auroral images. Mizuki Fukizawa analyzed the data prepared by co-authors and prepared the manuscript with contributions from all co-authors. Keisuke Hosokawa contributed to the discussion and interpretation of the analysis results.

340 **Competing interests**

At least one of the authors is a member of the editorial board of *Annales Geophysicae*.

Acknowledgements

The first author is a Research Fellow of the Japan Society for the Promotion of Science (JSPS). This study is supported by JSPS KAKENHI Grant Numbers JP17K05672, JP21H01152, and JP23KJ2145. EISCAT is an international association supported by research organizations in China (CRIRP), Finland (SA), Japan (NIPR), Norway (NFR), Sweden (VR), and the United Kingdom (UKRI). We thank Kellinsalmi Mirjam (Finnish Meteorological Institute) and Carl-Fredrik Enell (EISCAT Scientific Association) for maintaining the MIRACLE camera network and data flow. The database construction for the imager data at Skibotn and the EISCAT radar data has been supported by the IUGONET (Inter-university upper atmosphere Global Observation NETwork) project (<http://www.iugonet.org/>). The authors acknowledge the use of SuperDARN data.

345

350 SuperDARN is a collection of radars funded by national scientific funding agencies of Australia, Canada, China, France, Italy, Japan, Norway, South Africa, the United Kingdom, and the United States of America.

References

- Aso, T., Hashimoto, T., Abe, M., Ono, T. and Ejiri, M.: On the analysis of aurora stereo observations, *J. Geomagn. Geoelectr.*, 42(5), 579–595, doi:10.5636/jgg.42.579, 1990.
- 355 Aso, T., Gustavsson, B., Tanabe, K., Brändström, U., Sergienko, T. and Sandahl, I.: A proposed Bayesian model on the generalized tomographic inversion of aurora using multi-instrument data, *Proc. 33rd Annu. Eur. Meet. Atmos. Stud. by Opt. Methods, IRF Sci. Rep.*, (292), 105–109, 2008.
- Brekke, A.: *Physics of the Upper Polar Atmosphere (Second edition)*, 2013.
- Brown, N. B., Davis, T. N., Hallinan, T. J. and Stenbaek-Nielsen, H. C.: Altitude of pulsating aurora determined by a new instrumental technique, *Geophys. Res. Lett.*, 3(7), 403–404, doi:10.1029/GL003i007p00403, 1976.
- 360 Fujii, R., Oguti, T. and Yamamoto, T.: Relationships between pulsating auroras and field-aligned electric currents, *Mem. Natl. Inst. Polar Res. Spec. issue*, 36, 95–1003, 1985.
- Fukizawa, M., Sakanoi, T., Tanaka, Y., Ogawa, Y., Hosokawa, K., Gustavsson, B., Kauristie, K., Kozlovsky, A., Raita, T., Brandstrom, U. and Sergienko, T.: Reconstruction of precipitating electrons and three-dimensional structure of a pulsating auroral patch from monochromatic auroral images obtained from multiple observation points, *Ann. Geophys.*, 40, 475–484, doi:10.5194/angeo-40-475-2022, 2022.
- 365 Gillies, D. M., Knudsen, D., Spanswick, E., Donovan, E., Burchill, J. and Patrick, M.: Swarm observations of field-aligned currents associated with pulsating auroral patches, *J. Geophys. Res. A Sp. Phys.*, 120(11), 9484–9499, doi:10.1002/2015JA021416, 2015.
- 370 Gledhill, J. A.: The effective recombination coefficient of electrons in the ionosphere between 50 and 150 km, *Radio Sci.*, 21(3), 399–408, doi:10.1029/RS021i003p00399, 1986.
- Gordon, R., Bender, R. and Herman, G. T.: Algebraic Reconstruction Techniques (ART) for three-dimensional electron microscopy and X-ray photography, *J. Theor. Biol.*, 29(3), 471–481, doi:10.1016/0022-5193(70)90109-8, 1970.
- Greenwald, R. A., Baker, K. B., Dudeney, J. R., Pinnock, M., Jones, T. B., Thomas, E. C., Villain, J. P., Cerisier, J. C., 375 Senior, C., Hanuise, C., Hunsucker, R. D., Sofko, G., Koehler, J., Nielsen, E., Pellinen, R., Walker, A. D. M., Sato, N. and Yamagishi, H.: DARN/SuperDARN - A global view of the dynamics of high-latitude convection, *Space Sci. Rev.*, 71(1–4), 761–796, doi:10.1007/BF00751350/METRICS, 1995.
- Hosokawa, K. and Ogawa, Y.: Pedersen current carried by electrons in auroral D-region, *Geophys. Res. Lett.*, 37(18), 1–5, doi:10.1029/2010GL044746, 2010.
- 380 Hosokawa, K., Ogawa, Y., Kadokura, A., Miyaoka, H. and Sato, N.: Modulation of ionospheric conductance and electric field associated with pulsating aurora, *J. Geophys. Res. Sp. Phys.*, 115(3), 1–11, doi:10.1029/2009JA014683, 2010.

- Jones, A. V.: *Aurora*, D. Reidel Publishing Company, Dordrecht., 1974.
- 385 Kasahara, S., Miyoshi, Y., Yokota, S., Mitani, T., Kasahara, Y., Matsuda, S., Kumamoto, A., Matsuoka, A., Kazama, Y., Frey, H. U., Angelopoulos, V., Kurita, S., Keika, K., Seki, K. and Shinohara, I.: Pulsating aurora from electron scattering by chorus waves, *Nature*, 554(7692), 337–340, doi:10.1038/nature25505, 2018.
- Kawamura, M., Sakanoi, T., Fukizawa, M., Miyoshi, Y., Hosokawa, K., Tsuchiya, F., Katoh, Y., Ogawa, Y., Asamura, K., Saito, S., Spence, H., Johnson, A., Oyama, S. and Brändström, U.: Simultaneous pulsating aurora and microburst observations with ground-based fast auroral imagers and CubeSat FIREBIRD-II, *Geophys. Res. Lett.*, 48(18), 1–9, doi:10.1029/2021GL094494, 2021.
- 390 McEwen, D. J., Yee, E., Whalen, B. A. and Yau, A. W.: Electron energy measurements in pulsating auroras, *Can. J. Phys.*, 59(8), 1106–1115, doi:10.1139/p81-146, 1981.
- Miyoshi, Y., Katoh, Y., Nishiyama, T., Sakanoi, T., Asamura, K. and Hirahara, M.: Time of flight analysis of pulsating aurora electrons, considering wave-particle interactions with propagating whistler mode waves, *J. Geophys. Res. Sp. Phys.*, 115(10), 1–7, doi:10.1029/2009JA015127, 2010.
- 395 Miyoshi, Y., Oyama, S., Saito, S., Kurita, S., Fujiwara, H., Kataoka, R., Ebihara, Y., Kletzing, C., Reeves, G., Santolik, O., Clilverd, M., Rodger, C. J., Turunen, E. and Tsuchiya, F.: Energetic electron precipitation associated with pulsating aurora: EISCAT and Van Allen Probe observations, *J. Geophys. Res. Sp. Phys.*, 120, 2754–2766, doi:10.1002/2014JA020690., 2015.
- Miyoshi, Y., Saito, S., Kurita, S., Asamura, K., Hosokawa, K., Sakanoi, T., Mitani, T., Ogawa, Y., Oyama, S., Tsuchiya, F., 400 Jones, S. L., Jaynes, A. N. and Blake, J. B.: Relativistic electron microbursts as high-energy tail of pulsating aurora electrons, *Geophys. Res. Lett.*, 47(21), e2020GL090360, doi:10.1029/2020GL090360, 2020.
- Miyoshi, Y., Hosokawa, K., Kurita, S., Oyama, S. I., Ogawa, Y., Saito, S., Shinohara, I., Kero, A., Turunen, E., Verronen, P. T., Kasahara, S., Yokota, S., Mitani, T., Takashima, T., Higashio, N., Kasahara, Y., Matsuda, S., Tsuchiya, F., Kumamoto, A., Matsuoka, A., Hori, T., Keika, K., Shoji, M., Teramoto, M., Imajo, S., Jun, C. and Nakamura, S.: Penetration of MeV 405 electrons into the mesosphere accompanying pulsating aurorae, *Sci. Rep.*, 11(1), 1–9, doi:10.1038/s41598-021-92611-3, 2021.
- Nishimura, Y., Bortnik, J., Li, W., Thorne, R. M., Lyons, L. R., Angelopoulos, V., Mende, S. B., Bonnell, J. W., Le Contel, O., Cully, C., Ergun, R. and Auster, U.: Identifying the driver of pulsating aurora, *Science (80-.)*, 330(6000), 81–84, doi:10.1126/science.1193186, 2010.
- 410 Nishimura, Y., Bortnik, J., Li, W., Thorne, R. M., Chen, L., Lyons, L. R., Angelopoulos, V., Mende, S. B., Bonnell, J., Le Contel, O., Cully, C., Ergun, R. and Auster, U.: Multievent study of the correlation between pulsating aurora and whistler mode chorus emissions, *J. Geophys. Res. Sp. Phys.*, 116(11), 1–11, doi:10.1029/2011JA016876, 2011.
- Ogawa, Y., Tanaka, Y., Kadokura, A., Hosokawa, K., Ebihara, Y., Motoba, T., Gustavsson, B., Brändström, U., Sato, Y., Oyama, S., Ozaki, M., Raita, T., Sigernes, F., Nozawa, S., Shiokawa, K., Kosch, M., Kauristie, K., Hall, C., Suzuki, S., 415 Miyoshi, Y., Gerrard, A., Miyaoka, H. and Fujii, R.: Development of low-cost multi-wavelength imager system for studies

- of aurora and airglow, *Polar Sci.*, 23, doi:10.1016/j.polar.2019.100501, 2020a.
- Ogawa, Y., Kadokura, A. and Ejiri, M. K.: Optical calibration system of NIPR for aurora and airglow observations, *Polar Sci.*, 26, doi:10.1016/j.polar.2020.100570, 2020b.
- Oguti, T., Kokubun, S., Hayashi, K., Tsuruda, K., Machida, S., Kitamura, T., Saka, O. and Watanabe, T.: Statistics of pulsating auroras on the basis of all-sky TV data from five stations. I. Occurrence frequency, *Can. J. Phys.*, 59(8), 1150–1157, doi:10.1139/p81-152, 1981.
- Oguti, T., Meek, J. H. and Hayashi, K.: Multiple correlation between auroral and magnetic pulsations, *J. Geophys. Res.*, 89(A4), 2295–2303, doi:10.1029/JA089iA04p02295, 1984.
- Picone, J. M., Hedin, A. E., Drob, D. P. and Aikin, A. C.: NRLMSISE-00 empirical model of the atmosphere: Statistical comparisons and scientific issues, *J. Geophys. Res. Sp. Phys.*, 107(A12), 1468, doi:10.1029/2002JA009430, 2002.
- Rees, M. H. and Luckey, D.: Auroral electron energy derived from ratio of spectroscopic emissions 1. Model computations, *J. Geophys. Res.*, 79(34), 5181–5186, doi:10.1029/JA079i034p05181, 1974.
- Ritter, P., Lühr, H. and Rauberg, J.: Determining field-aligned currents with the Swarm constellation mission, *Earth, Planets Sp.*, 65(11), 1285–1294, doi:10.5047/eps.2013.09.006, 2013.
- Royrvik, O. and Davis, T. N.: Pulsating Aurora: Local and Global Morphology, *J. Geophys. Res.*, 82(29), 4720–4740, 1977.
- Sangalli, L., Partamies, N., Syrjäsoo, M., Enell, C. F., Kauristie, K. and Mäkinen, S.: Performance study of the new EMCCD-based all-sky cameras for auroral imaging, *Int. J. Remote Sens.*, 32(11), 2987–3003, doi:10.1080/01431161.2010.541505, 2011.
- Semeter, J. and Kamalabadi, F.: Determination of primary electron spectra from incoherent scatter radar measurements of the auroral E region, *Radio Sci.*, 40(2), n/a-n/a, doi:10.1029/2004RS003042, 2005.
- Shumko, M., Gallardo-Lacourt, B., Halford, A. J., Liang, J., Blum, L. W., Donovan, E., Murphy, K. R. and Spanswick, E.: A strong correlation between relativistic electron microbursts and patchy aurora, *Geophys. Res. Lett.*, 48(18), 1–10, doi:10.1029/2021GL094696, 2021.
- Solomon, S. C.: Global modeling of thermospheric airglow in the far ultraviolet, *J. Geophys. Res. Sp. Phys.*, 122(7), 7834–7848, doi:10.1002/2017JA024314, 2017.
- Stamm, J., Vierinen, J., Gustavsson, B. and Spicher, A.: A technique for volumetric incoherent scatter radar analysis, *Ann. Geophys.*, 41(1), 55–67, doi:10.5194/angeo-41-55-2023, 2023.
- Steele, D. P. and Mcewen, D. J.: Electron auroral excitation efficiencies and intensity ratios, *J. Geophys. Res.*, 95(A7), 10321–10336, doi:10.1029/JA095iA07p10321, 1990.
- Stone, M.: Cross-validators choice and assessment of statistical predictions (with discussion), *J. R. Stat. Soc. Ser. B*, 38(1), 102–102, doi:10.1111/j.2517-6161.1976.tb01573.x, 1974.
- Takahashi, T., Virtanen, I. I., Hosokawa, K., Ogawa, Y., Aikio, A., Miyaoka, H. and Kero, A.: Polarization electric field inside auroral patches: simultaneous experiment of EISCAT radars and KAIRA, *J. Geophys. Res. Sp. Phys.*, 124(5), 3543–3557, doi:10.1029/2018JA026254, 2019.

- 450 Tanabe, K.: Projection method for solving a singular system of linear equations and its applications, *Numer. Math.*, 17(3), 203–214, doi:10.1007/BF01436376, 1971.
- Tanaka, Y. M., Aso, T., Gustavsson, B., Tanabe, K., Ogawa, Y., Kadokura, A., Miyaoka, H., Sergienko, T., Brändström, U. and Sandahl, I.: Feasibility study on Generalized-Aurora Computed Tomography, *Ann. Geophys.*, 29(3), 551–562, doi:10.5194/angeo-29-551-2011, 2011.
- 455 Yamamoto, T.: On the temporal fluctuations of pulsating auroral luminosity, *J. Geophys. Res.*, 93(A2), 897–911, doi:10.1029/JA093iA02p00897, 1988.
- Yang, B., Donovan, E., Liang, J., Ruohoniemi, J. M. and Spanswick, E.: Using patchy pulsating aurora to remote sense magnetospheric convection, *Geophys. Res. Lett.*, 42(13), 5083–5089, doi:10.1002/2015GL064700, 2015.